

Preclinical Evaluation of ^{18}F -LMI1195 for In Vivo Imaging of Pheochromocytoma in the MENX Tumor Model

Florian C. Gaertner^{*1}, Tobias Wiedemann^{*2}, Behrooz H. Yousefi^{1,3}, Misu Lee², Ines Repokis², Takahiro Higuchi⁴, Stephan G. Nekolla¹, Ming Yu⁵, Simon Robinson⁵, Markus Schwaiger¹, and Natalia S. Pellegata²

¹Klinikum Rechts der Isar der Technischen Universität München, Nuklearmedizinische Klinik, München, Germany; ²Helmholtz Zentrum München, Deutsches Forschungszentrum für Gesundheit und Umwelt (GmbH), Institut für Pathologie, Neuherberg, Germany; ³Pharmaceutical Radiochemistry, Faculties of Chemistry and Medicine, Technische Universität München, Garching, Germany; ⁴Universitätsklinikum Würzburg, Comprehensive Heart Failure Center, Nuklearmedizinische Klinik und Poliklinik, Würzburg, Germany; and ⁵Discovery Research, Lantheus Medical Imaging, North Billerica, Massachusetts

We evaluated ^{18}F -LMI1195 (1-(3-bromo-4-(3- ^{18}F -fluoro-propoxy)benzyl)guanidine), a metaiodobenzylguanidine (MIBG) analog, for the detection of pheochromocytoma in a preclinical in vivo model of endogenous neuroendocrine tumors (multiple endocrine neoplasia [MENX]). **Methods:** Adrenal uptake kinetics of ^{18}F -LMI1195 were evaluated in healthy Wistar rats ($n = 6$) by dynamic PET imaging. Distribution of ^{18}F -LMI1195 was evaluated in tumor-bearing MENX mut/mut rats ($n = 10$) and control MENX wild-type rats ($n = 4$) by biodistribution studies and PET imaging. Biodistribution of ^{18}F -LMI1195 was compared with ^{123}I -MIBG in MENX mut/mut rats ($n = 6$) and correlated with histological tumor volume and norepinephrine transporter (NET) expression. Uptake specificity was evaluated by in vivo inhibition of the NET by desipramine ($n = 6$). Intraadrenal distribution of ^{18}F -LMI1195 was evaluated by autoradiography. **Results:** ^{18}F -LMI1195 showed rapid tracer accumulation in adrenal glands 1 min after tracer injection. Adrenal glands of MENX mut/mut animals showed significantly higher standardized uptake value than MENX wild-type controls (maximum SUV, 10.3 ± 2.3 vs. 6.1 ± 0.9 , $P < 0.01$). Adrenal uptake in MENX mut/mut rats could be inhibited by desipramine, shown by biodistribution studies (0.06 ± 0.01 vs. 0.16 ± 0.05 percentage injected dose, $P < 0.01$), PET imaging (maximum SUV, 3.8 ± 0.8 vs. 10.3 ± 2.3 , $P < 0.01$), and autoradiography. Adrenal uptake of ^{18}F -LMI1195 correlated with ^{123}I -MIBG uptake ($r = 0.91$), histological tumor volume ($r = 0.68$), and NET expression ($r = 0.50$). ^{18}F -LMI1195 showed an overall favorable distribution for tumor imaging. **Conclusion:** ^{18}F -LMI1195 shows high and specific accumulation in pheochromocytomas. Its favorable biodistribution makes it a promising PET tracer for tumor imaging. Further studies are warranted to evaluate its clinical value in oncologic indications.

Key Words: oncology; pheochromocytoma; MIBG; ^{18}F -LMI1195; MENX

J Nucl Med 2013; 54:2111–2117

DOI: 10.2967/jnumed.113.119966

Pheochromocytomas and paragangliomas are rare catecholamine-secreting neuroendocrine tumors arising from chromaffin cells of the adrenal medulla and sympathetic ganglia. Malignant transformation occurs in up to 10%. The overall 5-y survival rate of malignant pheochromocytomas is approximately 50%, and once metastasized, there is no curative treatment for this disease (1,2). Therefore, early diagnosis and precise localization of pheochromocytomas and their metastases is crucial for successful therapy.

Diagnosis of pheochromocytoma involves measurement of catecholamines and their metabolites at the biochemical level and anatomic imaging, such as CT and MR tomography (MRT), at the macroscopic level. Functional imaging can be performed using radioiodinated metaiodobenzylguanidine (MIBG) for planar scintigraphy and SPECT, offering high sensitivity and specificity (3). Tumor uptake of MIBG is mediated by the norepinephrine transporter (NET), which is abundant on the surface of pheochromocytoma cells (3).

However, shortcomings on the pharmacokinetic side (e.g., physiologic background activity in the liver) and on the physical side (e.g., low spatial resolution and inaccurate attenuation correction of the SPECT technique) compromise the image quality of MIBG SPECT (4). These shortcomings might be overcome by PET radiopharmaceuticals. For example, ^{11}C -meta-hydroxyephedrine (^{11}C -HED) (5) and ^{18}F -6-fluorodopamine (^{18}F -FDA) (6), both targeting the NET, are able to detect pheochromocytomas in vivo. However, the short half-life of ^{11}C -HED (20 min) limits its widespread routine application, and the clinical availability of ^{18}F -FDA is limited because of its complex radiosynthesis (3). The PET tracers ^{18}F -L-6-fluoro-3,4-dihydroxyphenylalanine (^{18}F -DOPA), targeting the aromatic amino acid transporter and L-amino acid decarboxylase (3,7,8), and ^{68}Ga -labeled somatostatin analogs (e.g., ^{68}Ga -DOTATOC and ^{68}Ga -DOTATATE), targeting somatostatin receptors (9), can also be used to visualize pheochromocytomas. However, because of their different mechanism of action, these tracers deliver a different quality of information from MIBG.

^{18}F -LMI1195 (1-(3-bromo-4-(3-fluoro-propoxy)benzyl)guanidine) is a novel MIBG analog PET tracer for imaging of NET activity. ^{18}F -LMI1195 has already shown promising results in the imaging of cardiac sympathetic innervation (4,10); however, its feasibility for tumor imaging has not yet been evaluated in vivo.

In the current study, we used the multiple endocrine neoplasia (MENX) animal model for in vivo imaging of pheochromocytomas with ^{18}F -LMI1195. The MENX syndrome is caused by

Received Jan. 14, 2013; revision accepted Jul. 9, 2013.

For correspondence or reprints contact: Florian C. Gaertner, Klinikum Rechts der Isar der Technischen Universität München, Nuklearmedizinische Klinik und Poliklinik, Ismaninger Strasse 22, 81675 München, Germany.

E-mail: florian.gaertner@tum.de

*Contributed equally to this work.

Published online Oct. 17, 2013.

COPYRIGHT © 2013 by the Society of Nuclear Medicine and Molecular Imaging, Inc.

a homozygous germline mutation in the cell cycle regulatory gene *Cdkn1b*, encoding p27Kip1 (11), leading to development of bilateral pheochromocytomas with 100% penetrance. These tumors show a clear progression from adrenal medullary hyperplasia to adenoma (12) and closely resemble their human counterpart at the histopathological and molecular level (13). Previously, we have shown that ^{11}C -HED and ^{68}Ga -DOTATOC can be used for the detection of MENX-associated pheochromocytoma in vivo (14).

We here evaluated ^{18}F -LMI1195 for the detection of pheochromocytoma in MENX-affected rats. To our knowledge, this is the first feasibility study of ^{18}F -LMI1195 for in vivo tumor imaging.

MATERIALS AND METHODS

Animals, Radiotracers, and Chemicals

MENX-affected Sprague–Dawley rats (hereafter indicated as mut/mut) were maintained as previously reported (12). MENX control rats are wild-type rats derived from this strain. Wistar control rats were from Charles River Laboratories. Animals were maintained and treated in agreement with the procedures approved by the Helmholtz Zentrum München, by the Technische Universität München, and by the local government authorities (Bayerische Landesregierung).

LMI1195 precursor and the method for radiosynthesis of ^{18}F -LMI1195 were provided by Lantheus Medical Imaging as described previously (4). The radiochemical purity of ^{18}F -LMI1195 was 98% or greater, and the specific activity was greater than 600 GBq/ μmol . ^{123}I -MIBG was from GE Healthcare (specific activity, 8 TBq/ μmol , according to the manufacturer). Desipramine was from Sigma-Aldrich.

Tracer Injection and PET Imaging

Animals were anesthetized by 2% isoflurane inhalation and injected with 21.8 ± 3.9 MBq of ^{18}F -LMI1195 via the tail vein. For ^{18}F -LMI1195 and ^{123}I -MIBG coinjection studies, animals were injected with 1.08 ± 0.05 MBq of ^{123}I -MIBG immediately after injection of ^{18}F -LMI1195. For blocking experiments, animals were injected intravenously with desipramine (10 mg/kg) 10 min before tracer injection. PET was performed using a dedicated small-animal PET scanner (Inveon Micro PET/CT; Siemens Preclinical Solutions). Dynamic PET scans were reconstructed using 12 frames of 15 s and 57 frames of 60 s. Static PET scans were started 45 min after tracer injection; emission time was 15 min. PET data were reconstructed using 2-dimensional ordered-subset expectation maximization. Images were corrected for decay, randoms, and dead time. Attenuation and scatter correction was not performed.

PET images were analyzed using a dedicated workstation (Inveon Research Workplace, version 4.0; Siemens Preclinical Solutions). Spheric volumes of interest were placed around the hottest voxel of the adrenals (20 pixel [px]), in the liver (40 px), in the psoas muscle (40 px), and in the lumen of the left ventricle (10 px). Standardized uptake values (SUVs) were calculated by $\text{SUV} = (\text{measured activity [Bq/mL]} \times (\text{body weight [g]})) \div (\text{injected activity [Bq]})$.

Additionally, partial-volume correction was applied to the maximum SUV (SUV_{max}) of the adrenal glands. Digital sphere phantoms with different volumes were generated to measure recovery coefficients using a combined SimSET (Simulation System for Emission Tomography) and GATE (Geant4 Application for Tomography Emission) Monte Carlo simulation method. PET sinograms were generated using the geometry of the scintillators and the detector circuitry of the Siemens Inveon scanner (15).

Biodistribution

Animals were euthanized by intravenous injection of sodium pentobarbital (100 mg/kg of body weight) (Narcoren; Merial GmbH) and subjected to complete necropsy.

^{18}F samples were analyzed using a single-well counter (Wizard 1460; Wallac) for 60 s (energy window, 400–600 keV). Activity of ^{123}I was determined 24 h later (energy window, 135–172 keV, 60 s counting time) while correcting the previously measured ^{18}F samples for ^{123}I -crosstalk (crosstalk fraction, 0.3%). Bone activity was measured including bone marrow.

Radioactivity (cpm) was normalized to organ weight (g), injected activity (cpm), and body weight (kg). Normalization to body weight was performed because, due to their physiology, the body weight of MENX wild-type control animals tends to be lower than the body weight of mut/mut animals. Tracer biodistribution is expressed as percentage of injected dose per gram of tissue multiplied by body weight ($\% \text{ID/g} \times \text{kg}$).

In mut/mut animals, the pheochromocytoma is microscopically embedded in the adrenal medulla, and tissue separation for separate activity measurement of the pheochromocytoma is not feasible. Therefore, adrenal activity accumulation in mut/mut animals comprises a mixture of tumor uptake plus remaining adrenal medulla and cortex and does not represent solely tumor uptake. Normalization to organ weight is not meaningful in this case. Therefore, no normalization to organ and body weight was performed for the adrenal glands, and adrenal tracer accumulation is given as percentage of injected dose ($\% \text{ID}$).

Autoradiography

Organs were frozen in liquid nitrogen. Cryosections (8 and 20 μm) were generated (HM 500 OM; Microm Laborgeräte) and thaw-mounted onto microscope slides (Thermo Scientific SupraFrost Ultra Plus; Menzel GmbH). The 8- μm cryosections were stained with hematoxylin and eosin (H&E) and examined under a light microscope (BZ 9000; Keyence). The 20- μm cryosections were exposed to a phosphor imaging plate (Storage Phosphor Screen GP; Kodak) for 16 h, which was scanned subsequently (CR 35 Bio; Raytest). Densitometry was performed using the software ImageJ (version 1.46; National Institutes of Health). Regions of interest (ROIs) were created corresponding to the adrenal medulla outlined in the H&E-stained sections. Reference ROIs were placed in an area of homogeneous activity of the adrenal cortex. The ratio of medulla to cortex was calculated by dividing the average pixel value of the medullary ROI by the average pixel value of the cortical ROI.

Histological Analysis, RNA Extraction, and Real-Time Reverse Transcription Polymerase Chain Reaction (RT-PCR)

Adrenal glands not undergoing autoradiography were formalin-fixed, paraffin-embedded, and stained with H&E. The ellipsoid formula was used to calculate the tumor volume, with the shortest diameter as the third dimension.

RNA was extracted as previously reported (16). Real-time quantitative RT-PCR was performed using TaqMan Assay-on-Demand primers and probes for the norepinephrine transporter (*Slc6a2*) gene and for the β 2-microglobulin (*B2M*) housekeeping gene as internal control (Applied Biosystems).

Statistical Methods

The 2-tailed Mann–Whitney *U* test (SPSS Statistics, version 17; SPSS, Inc.) was used to evaluate the significance of differences between 2 samples. The Pearson correlation coefficient was used to test the correlation between adrenal uptake of ^{18}F -LMI1195 and ^{123}I -MIBG uptake, adrenal weight, NET expression, and tumor volume.

RESULTS

Pharmacokinetics of ^{18}F -LMI1195 in Wistar Control Rats

Dynamic PET measurements of ^{18}F -LMI1195 after intravenous injection in healthy Wistar control rats ($n = 6$) showed rapid tracer accumulation in the adrenal glands (Figs. 1A and 1B). Maximum uptake was reached 1 min after injection and remained high for 60 min, showing only discrete washout. Muscle background activity reached

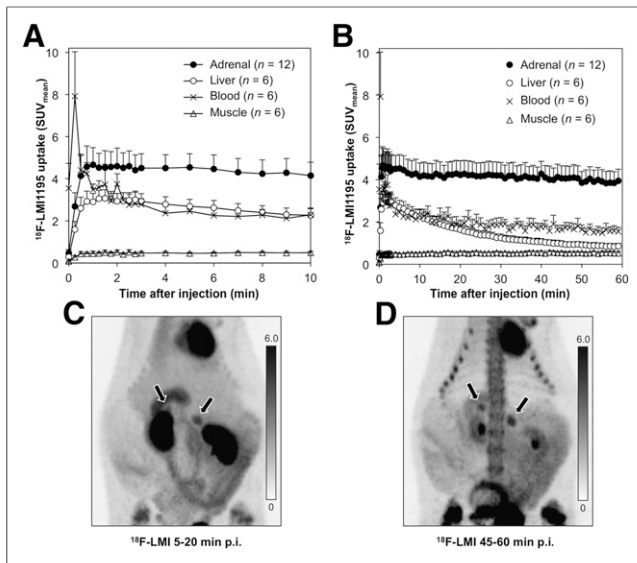


FIGURE 1. (A and B) Pharmacokinetics of ¹⁸F-LMI1195 in healthy Wistar control rats ($n = 6$), evaluated by dynamic PET imaging. Maximal adrenal uptake was reached 1 min after injection. Background organs reached low activity after approximately 45 min. (C and D) Maximum-intensity projection of PET images 5 and 45 min after injection. Scale bars represent SUV. Adrenal glands (arrows) can already be delineated well in early PET images (C). Late images show lower background activity; however, bone uptake is increased (D). p.i. = after injection.

a low plateau 1 min after injection. Blood activity showed a peak at about 15 s after injection, followed by a rapid decline up to 3 min after injection and a slower decrease during the remaining time period. Liver uptake showed a peak at about 1–3 min after injection, followed by a rapid tracer washout, reaching low levels about 45 min after injection.

By visual analysis, adrenal glands could be delineated clearly in the early PET images 5–20 min after injection (Fig. 1C; Supplemental Fig. 1A [supplemental materials are available at <http://jnm.snmjournals.org>]). In later PET images, 45–60 min after injection, adrenal-to-background contrast increased because of tracer washout from background tissues, especially from the liver, renal cortex, and upper gastrointestinal tract (Fig. 1D; Supplemental Fig. 1B). Prominent bone uptake was observed at late time points.

PET Imaging of ¹⁸F-LMI1195 in MENX Wild-Type and mut/mut Rats

Static PET imaging was performed 45 min after injection of ¹⁸F-LMI1195 in healthy MENX wild-type rats ($n = 4$), tumor-bearing mut/mut rats ($n = 10$), and mut/mut rats after previous inhibition of the NET with desipramine ($n = 6$). By visual analysis, adrenal-to-background contrast was considerably higher in nonblocked mut/mut animals than in wild-type rats, whereas tracer distribution in the other organs was nearly identical (Figs. 2A and 2B). After desipramine injection, adrenal-to-background contrast was strikingly lower, liver uptake was higher, and bone uptake was lower compared with nonblocked mut/mut rats (Fig. 2C).

Quantitative image analysis revealed significantly higher SUV_{max} and mean SUV (SUV_{mean}) in the adrenal glands of mut/mut animals than in wild-type controls (SUV_{max} , 10.3 ± 2.3 vs. 6.1 ± 0.9 , $P < 0.01$; SUV_{mean} , 7.4 ± 1.7 vs. 4.2 ± 0.8 , $P < 0.01$). Similar results were obtained for SUV_{max} of the adrenal glands when partial-volume correction ($SUV_{max(PV)}$, 10.8 ± 2.4 vs. 7.4 ± 1.1 , $P < 0.01$)

was also performed (Fig. 2D). The SUV_{mean} of liver, muscle, and blood did not differ significantly between mut/mut rats and wild-type controls ($P > 0.05$). After desipramine treatment, significantly lower SUVs were observed in the adrenal glands of blocked mut/mut rats than nonblocked mut/mut animals (SUV_{max} , 3.8 ± 0.8 vs. 10.3 ± 2.3 , $P < 0.01$; SUV_{mean} , 2.9 ± 0.6 vs. 7.4 ± 1.7 , $P < 0.01$). Partial-volume-corrected SUV_{max} of the adrenal glands showed similar results ($SUV_{max(PV)}$, 4.2 ± 0.7 vs. 10.8 ± 2.4 , $P < 0.01$). SUV_{mean} of the liver was significantly higher in blocked MENX mut/mut rats (SUV_{mean} , 3.0 ± 0.8 vs. 0.7 ± 0.1 , $P < 0.01$), whereas there were no significant differences in SUV_{mean} for muscle (0.3 ± 0.1 vs. 0.4 ± 0.1 , $P > 0.05$) and blood (1.1 ± 0.4 vs. 1.1 ± 0.4 , $P > 0.05$).

Evaluation of the interscapular brown adipose tissue (BAT) showed highly variable ¹⁸F-LMI1195 accumulation, with no significant differences in SUV between mut/mut and wild-type rats. Higher BAT SUVs were usually observed after desipramine treatment.

Autoradiography

Autoradiography of ¹⁸F-LMI1195 distribution was performed for muscle tissue (serving as negative control), 1 adrenal gland of a MENX wild-type control rat, the adrenal glands of a nonblocked mut/mut rat, and those of a mut/mut rat after desipramine treatment. No tracer accumulation was observed in muscle tissue (not shown). Control adrenal glands of wild-type animals showed low uptake in the medulla and in the outer margin of the cortex. Adrenal glands of nonblocked mut/mut rats showed inhomogeneous uptake in the enlarged adrenal medulla, with some focal areas of high tracer accumulation, corresponding to the pheochromocytoma. In contrast, adrenal glands of desipramine-treated mut/mut animals did not exhibit areas of increased tracer uptake. In these animals, virtually no tracer accumulation was observed in the area of the pheochromocytoma (Fig. 3A).

Activity accumulation in the adrenal medulla was evaluated by densitometry in the wild-type control rat (1 slice), in the tumor-bearing mut/mut rat (2 slices), and in the desipramine-blocked mut/mut rat (2 slices). The mean ratio of medulla to cortex was considerably increased in the nonblocked mut/mut animal, compared with the control rat (ratio, 3.31 vs. 1.99), and showed a distinct decrease after desipramine treatment (ratio, 1.59) (Fig. 3B).

Biodistribution of ¹⁸F-LMI1195 in MENX Wild-Type and MENX mut/mut Rats

The biodistribution of ¹⁸F-LMI1195 was evaluated 60 min after tracer injection in wild-type control rats ($n = 4$), tumor-bearing mut/mut rats ($n = 10$), and mut/mut rats after previous inhibition of the NET with desipramine ($n = 6$) (Fig. 4).

When nonblocked mut/mut rats were compared with wild-type controls, total radioactivity in the adrenal glands (%ID) was significantly higher in mut/mut animals (0.16 ± 0.05 %ID vs. 0.09 ± 0.02 %ID, $P < 0.01$). Furthermore, significant differences were observed for blood and kidneys. There were no significant differences regarding the other tissue types evaluated ($P > 0.05$).

After desipramine treatment, tracer accumulation in the adrenal glands was significantly reduced, compared with nonblocked mut/mut animals (0.06 ± 0.01 %ID vs. 0.16 ± 0.05 %ID, $P < 0.01$). After desipramine treatment, tracer uptake in the liver was increased about 6–7 times (0.34 ± 0.07 %ID/g \times kg vs. 0.05 ± 0.01 %ID/g \times kg, $P < 0.01$). Further significant differences were observed for the kidneys, spleen, and bone.

Detailed results of ¹⁸F-LMI1195 biodistribution in MENX wild-type, nonblocked, and blocked mut/mut animals are listed in Table 1.

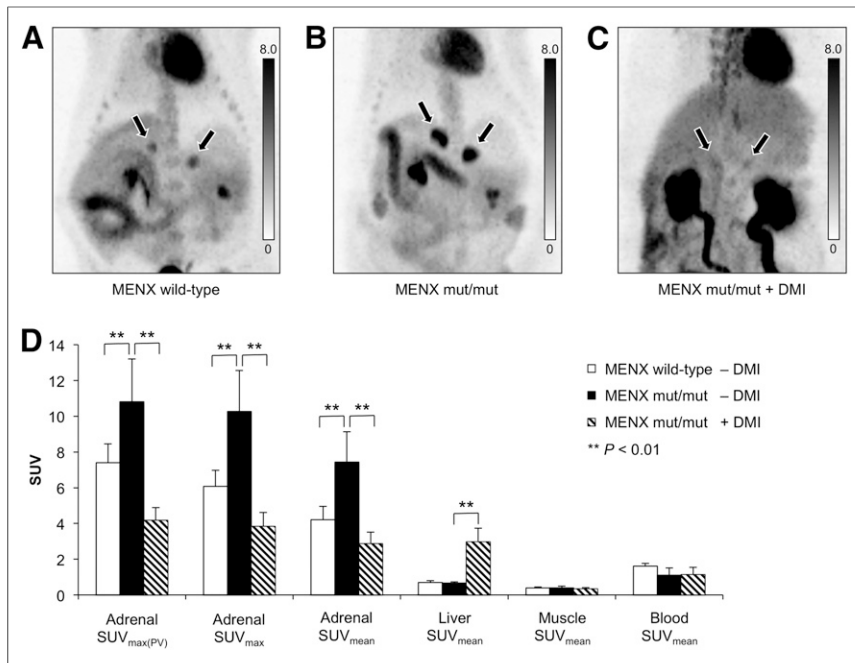


FIGURE 2. (A–C) ^{18}F -LMI1195 PET images (maximum-intensity projection) 45 min after injection. Scale bars represent SUV. Normal adrenal glands of MENX wild-type rat show moderate tracer accumulation (A), whereas intense tracer accumulation is observed in adrenal glands of tumor-bearing mut/mut rat (B). After inhibition of NET with desipramine (DMI), tracer uptake in adrenal glands is significantly reduced (C). (D) Quantitative ^{18}F -LMI1195 PET analysis of MENX wild-type control rats ($n = 4$), mut/mut rats ($n = 10$), and mut/mut rats after inhibition of NET with desipramine ($n = 6$). Bars represent mean SUV_{max} corrected for partial volume (SUV_{max(PV)}), mean SUV_{max}, or mean SUV_{mean} as indicated in legend. Error bars represent SD. SUV of adrenal glands of mut/mut animals were significantly higher than those of wild-type controls ($P < 0.01$). After desipramine treatment, SUV of adrenal glands decreased significantly ($P < 0.01$), whereas significantly higher SUV was observed in liver ($P < 0.01$).

Comparison of ^{18}F -LMI1195 with ^{123}I -MIBG in MENX mut/mut Rats

The biodistribution of ^{123}I -MIBG was evaluated in MENX mut/mut rats 60 min after tracer injection ($n = 6$). No significant

differences in tracer uptake were observed in the adrenal glands, compared with ^{18}F -LMI1195 (0.15 ± 0.03 %ID vs. 0.16 ± 0.05 %ID, $P > 0.05$) (Fig. 5A). Liver uptake of ^{123}I -MIBG was significantly higher than ^{18}F -LMI1195 (0.30 ± 0.03 %ID/g \times kg vs. 0.05 ± 0.01 %ID/g \times kg, $P < 0.01$) (Fig. 5B). Furthermore, significant differences were observed in the kidneys, spleen, muscle, small intestine, brain, and lung. Detailed results of the biodistribution of ^{123}I -MIBG are listed in Table 1.

In 6 mut/mut rats, tracer distribution of ^{18}F -LMI1195 and ^{123}I -MIBG was evaluated 60 min after coinjection by dual-radionuclide tissue counting. Uptake of ^{18}F -LMI1195 and ^{123}I -MIBG in the adrenal glands showed a strong and linear correlation (Pearson correlation coefficient, $r = 0.91$) (Supplemental Fig. 2).

There was no correlation between ^{18}F -LMI1195 uptake (SUV_{max} and SUV_{mean}) and adrenal weight (Pearson correlation coefficient, $r = -0.021$, SUV_{max} [Supplemental Fig. 3A] and 0.037 , SUV_{mean} [not shown]). A moderate correlation was observed between SUV_{max}/SUV_{mean} and expression levels

Correlation of ^{18}F -LMI1195 Uptake with Adrenal Weight, NET Expression, and Tumor Volume

of the NET gene (*Slc6a2*), as determined by real-time quantitative RT-PCR, with a Pearson correlation coefficient of 0.501 (SUV_{max}, Supplemental Fig. 3B) and 0.488 (SUV_{mean}, not shown). A good correlation was observed between SUV_{max}/SUV_{mean} and histological tumor volume (Pearson correlation coefficient, $r = 0.679$, SUV_{max} [Supplemental Fig. 3C] and 0.643 , SUV_{mean} [not shown]). Similar results were obtained when additional partial-volume correction for SUV_{max} of the adrenal glands was performed; in these cases Pearson correlation coefficients were -0.138 for adrenal weight (Supplemental Fig. 3D), 0.513 for NET expression (Supplemental Fig. 3E), and 0.656 for histological tumor volume (Supplemental Fig. 3F).

DISCUSSION

Overall our results show that the catecholamine analog ^{18}F -LMI1195 is a suitable PET tracer for the in vivo detection of pheochromocytoma. ^{18}F -LMI1195 showed significantly higher SUVs in tumor-bearing adrenal glands of MENX mut/mut rats than wild-type controls.

Because uptake of catecholamines in pheochromocytomas is mediated by overexpression of the NET (3), and previous in vitro

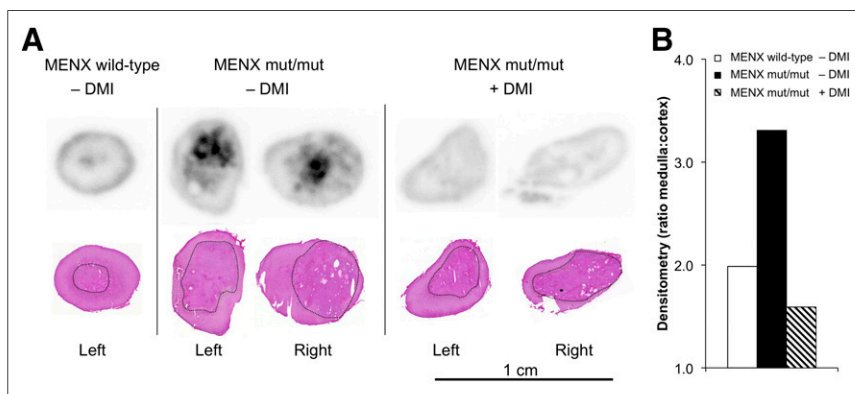


FIGURE 3. (A) Autoradiography of adrenal glands 60 min after injection of ^{18}F -LMI1195 (top) and corresponding H&E stained slices (bottom). Low tracer uptake is observed in adrenal medulla (black outline in H&E staining) and in outer margin of adrenal cortex of wild-type control animal (left). Inhomogeneous tracer uptake is observed in enlarged adrenal medulla of tumor-bearing mut/mut rat, with focal areas of high tracer accumulation (middle). After desipramine (DMI) injection, virtually no tracer uptake is observed in area of pheochromocytoma in mut/mut animals (right). (B) Densitometry of autoradiography slices shown in A. Bars represent ratio of medulla to cortex of wild-type rat ($n = 1$), mean ratio of mut/mut animal ($n = 2$), and mean ratio of desipramine-blocked mut/mut rat ($n = 2$).

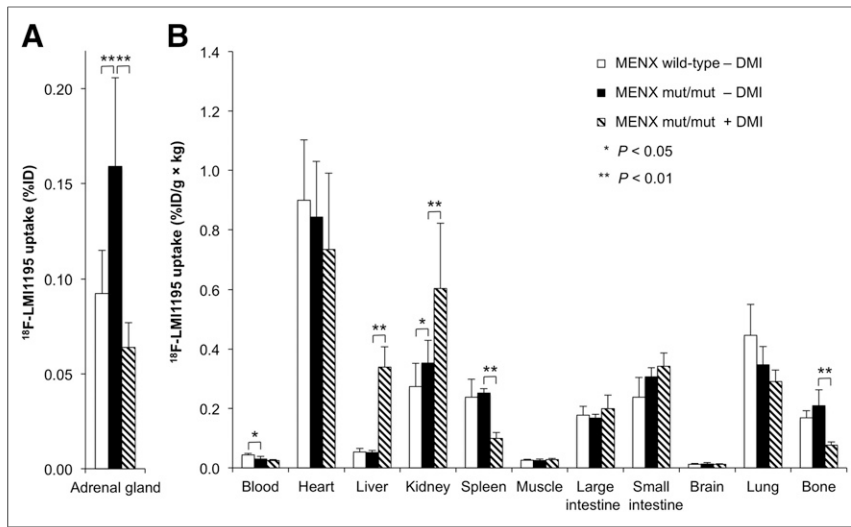


FIGURE 4. Biodistribution 60 min after injection of ^{18}F -LMI1195 in MENX wild-type control rats ($n = 4$), mut/mut rats ($n = 10$), and mut/mut rats after desipramine (DMI) treatment ($n = 6$). (A) Bars represent total tracer uptake in adrenal glands (%ID), and error bars represent SD. (B) Bars represent tracer uptake in remaining organs normalized to organ weight and body weight, and error bars represent SD. When wild-type and nonblocked mut/mut rats were compared, total activity of ^{18}F -LMI1195 in adrenal glands of mut/mut rats was significantly higher (A, $P < 0.01$). Furthermore, significant differences were observed for blood and kidneys (B). When nonblocked and blocked mut/mut rats were compared, tracer accumulation in adrenal glands was significantly lower in blocked animals (A). Tracer uptake in liver was significantly higher after desipramine treatment (B). Further significant differences were observed for kidneys, spleen, and bone.

reports have already shown comparable uptake kinetics (K_i [affinity], K_m [Michaelis-Menten constant], and V_{max} [maximum rate]) of the NET for norepinephrine and ^{19}F -LMI1195 (4), our current in vivo results are consistent with the previously published in vitro

data. Furthermore, we observed a moderate correlation between ^{18}F -LMI1195 uptake and expression of the NET gene (*Slc6a2*), supporting specificity of tracer uptake. Quantitative assessment of NET expression on the protein level would have represented a better surrogate for cellular norepinephrine uptake activity, but unfortunately the results of immunohistochemical staining of rat tissues with an anti-NET antibody were not reliable and are therefore not shown.

Although no correlation was observed between adrenal weight and uptake of ^{18}F -LMI1195 in mut/mut rats, there was a positive correlation between tracer uptake and tumor volume assessed by histology. This corroborates tumor-specific tracer accumulation in the adrenal glands of mut/mut rats. Because of this correlation, we hypothesized that ^{18}F -LMI1195 might be suitable for not only tumor detection but also assessment of tumor burden, which could be useful for disease monitoring and therapy response assessment.

Previous in vitro reports have shown that the selective NET inhibitor desipramine (inhibition of the neuronal uptake-1 mechanism) significantly decreases uptake of ^{18}F -LMI1195 in the human neuroblastoma cell line SK-N-SH (10). In line with these reports, we observed a significant reduction of ^{18}F -LMI1195 uptake in the adrenal glands of mut/mut animals after desipramine treatment in vivo. Consistently, whereas autoradiography showed

Consistently, whereas autoradiography showed

TABLE 1
Biodistribution of ^{18}F -LMI1195 and ^{123}I -MIBG in MENX Wild-Type Rats and MENX mut/mut Rats With and Without Previous Blocking of NET With Desipramine

Parameter	^{18}F -LMI1195			^{123}I -MIBG, MENX mut/mut
	MENX wild-type	MENX mut/mut	MENX mut/mut	
Time after injection	60 min	60 min	60 min	60 min
Blocking	None	None	Desipramine, 10 mg/kg	None
No. of rats	4	10	6	6
Animal weight	358 ± 101 g	445 ± 95 g	450 ± 115 g	443 ± 99 g
Organ (%ID/g × kg)				
Blood	0.044 ± 0.005	0.030 ± 0.008 ($P = 0.024^*$)	0.024 ± 0.003 ($P = 0.18$)	0.035 ± 0.008 ($P = 0.23$)
Heart	0.90 ± 0.20	0.84 ± 0.19 ($P = 0.57$)	0.73 ± 0.26 ($P = 0.42$)	0.83 ± 0.11 ($P = 0.59$)
Liver	0.053 ± 0.012	0.051 ± 0.007 ($P = 0.78$)	0.34 ± 0.068 ($P < 0.001^*$)	0.300 ± 0.025 ($P = 0.001^*$)
Kidney	0.27 ± 0.079	0.35 ± 0.076 ($P = 0.025^*$)	0.60 ± 0.22 ($P = 0.002^*$)	0.29 ± 0.12 ($P = 0.038^*$)
Spleen	0.24 ± 0.060	0.25 ± 0.015 ($P = 0.83$)	0.10 ± 0.020 ($P = 0.002^*$)	0.28 ± 0.019 ($P = 0.009^*$)
Muscle	0.026 ± 0.003	0.025 ± 0.005 ($P = 0.48$)	0.027 ± 0.004 ($P = 0.26$)	0.020 ± 0.002 ($P = 0.009^*$)
Large intestine	0.18 ± 0.030	0.17 ± 0.012 ($P = 0.39$)	0.20 ± 0.046 ($P = 0.39$)	0.17 ± 0.014 ($P = 0.52$)
Small intestine	0.24 ± 0.067	0.31 ± 0.030 ($P = 0.088$)	0.34 ± 0.046 ($P = 0.18$)	0.43 ± 0.084 ($P = 0.006^*$)
Brain	0.012 ± 0.003	0.012 ± 0.005 ($P = 0.67$)	0.012 ± 0.003 ($P = 1.0$)	0.006 ± 0.003 ($P = 0.037^*$)
Lung	0.45 ± 0.11	0.35 ± 0.062 ($P = 0.20$)	0.29 ± 0.039 ($P = 0.18$)	0.56 ± 0.10 ($P = 0.006^*$)
Bone	0.17 ± 0.024	0.21 ± 0.054 ($P = 0.20$)	0.077 ± 0.010 ($P = 0.002^*$)	0.034 ± 0.006 ($P = 0.004^*$)
Adrenal gland (%ID)	0.092 ± 0.023	0.16 ± 0.047 ($P < 0.001^*$)	0.064 ± 0.013 ($P < 0.001^*$)	0.15 ± 0.028 ($P = 0.60$)

*Significant P values.

Biodistribution values are %ID ± SD for adrenal glands and %ID/g × kg ± SD for other organs. P values for nonblocked ^{18}F -LMI1195 in MENX mut/mut rats are with respect to ^{18}F -LMI1195 in wild-type rats. P values for other 2 categories are with respect to nonblocked ^{18}F -LMI1195 in mut/mut rats.

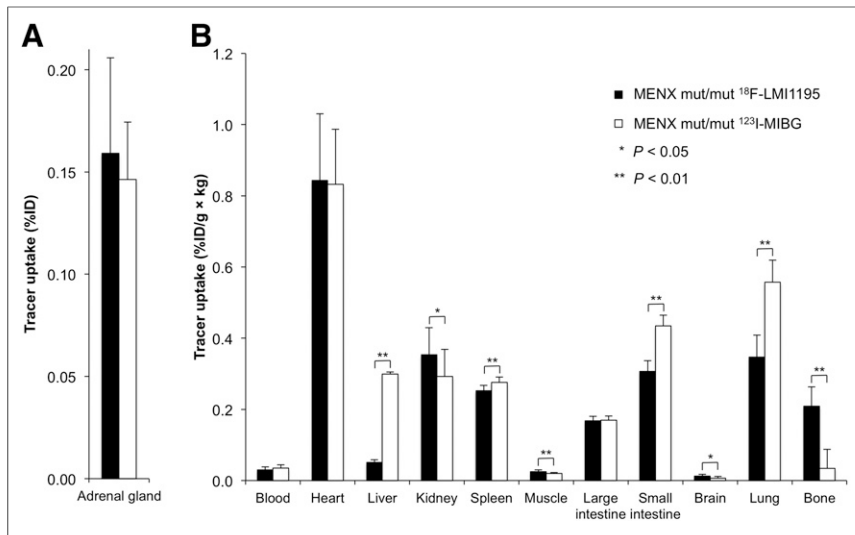


FIGURE 5. Biodistribution of ^{18}F -LMI1195 ($n = 10$) and ^{123}I -MIBG ($n = 6$) in tumor-bearing mut/mut rats (60 min after injection). (A) Bars represent total tracer uptake in adrenal glands, and error bars represent SD. No significant differences are observed in adrenal tracer uptake between ^{18}F -LMI1195 and ^{123}I -MIBG ($P > 0.05$). (B) Bars represent tracer uptake in remaining organs normalized to organ weight and body weight, and error bars represent SD. Liver uptake of ^{18}F -LMI1195 was significantly lower than ^{123}I -MIBG ($P < 0.01$), whereas bone uptake was significantly higher ($P < 0.01$). Furthermore, significant differences were observed regarding kidneys, spleen, muscle, small intestine, brain, and lung.

areas of intensely enhanced tracer uptake in the adrenal medulla of nonblocked mut/mut rats, these tumor areas did not show evidence of tracer accumulation after desipramine treatment, underlining the predominance of the neuronal uptake-1 mechanism in the MENX pheochromocytoma model.

A reduction of ^{18}F -LMI1195 uptake was also observed in the spleen after inhibition of the NET with desipramine, indicating uptake-1-mediated accumulation of ^{18}F -LMI1195 in this organ too. This is consistent with reports suggesting sympathetic innervation of the spleen (17).

Previous publications have shown specific inhibition of neuronal cardiac uptake of ^{18}F -LMI1195 in rabbits and nonhuman primates by desipramine (4). However, recent data show that desipramine is unable to significantly inhibit cardiac uptake of ^{18}F -LMI1195 (18) or its analog MIBG (19) in rats. Our results are in agreement with these latest findings. The discrepant results obtained in rats versus rabbits and primates are probably caused by interspecies differences in cardiac catecholamine handling, with a predominance of the nonneuronal uptake-2 mechanism in rat hearts, which is not inhibited by desipramine (18).

It has been previously shown that in vitro uptake of ^{18}F -LMI1195 is comparable to its analog ^{123}I -MIBG in the human neuroblastoma cell line SK-N-SH (10). In line with these results, we observed a strong and linear correlation between ^{18}F -LMI1195 and ^{123}I -MIBG uptake in the adrenal glands of mut/mut rats in vivo, substantiating our hypothesis that ^{18}F -LMI1195 might constitute a sensitive and specific PET tracer for detection and staging of pheochromocytoma in patients, similarly to ^{123}I -MIBG and ^{131}I -MIBG, which are clinically established SPECT tracers for patient imaging (3). In the clinical setting, higher diagnostic accuracy of ^{18}F -LMI1195 PET might be expected, compared with scintigraphy or SPECT with MIBG, because PET offers several advantages, including higher spatial resolution, higher sensitivity, the possibility of absolute quantification, and feasibility of whole-body tomographic imaging in patients (20,21).

^{18}F -LMI1195 shows favorable pharmacokinetics for PET imaging, leading to clear visualization of pheochromocytomas in the MENX model about 1 h after tracer injection, a time period comparable to clinically established PET tracers (e.g., ^{18}F -FDG). In contrast, image acquisition is typically performed up to 24 and 48 h after injection of ^{123}I -MIBG or ^{131}I -MIBG, respectively, leading to more complex and laborious clinical scan protocols. ^{18}F -LMI1195 showed background uptake in the liver, lung, and small intestine, which was significantly lower than that observed for ^{123}I -MIBG. This finding is consistent with previous publications reporting a lower uptake of ^{18}F -LMI1195 in the liver and lung in rats and nonhuman primates (4). The lower uptake in the liver and small intestine might be advantageous for detection of the primary tumors, abdominal lymph node metastases, and liver metastases. The lower uptake in lung tissue may be useful for the detection of pulmonary metastases. In contrast to ^{123}I -MIBG, significant radioactivity accumulation was observed in the bone after injection of ^{18}F -LMI1195,

especially at later time points. However, because bone was measured together with the bone marrow, these 2 compartments cannot be distinguished. Metabolic degradation of ^{18}F -LMI1195 (e.g., defluorination) might be the cause of bone accumulation. However, metabolites were not examined in the current study, so that this issue still needs to be addressed. It is hard to predict whether bone uptake of ^{18}F -LMI1195 will (negatively or positively) affect the detectability of bone metastasis in the clinical setting.

In addition to ^{18}F -LMI1195, other PET tracers targeting the NET have been developed which accumulate in pheochromocytomas, for example, ^{11}C -HED (5) and ^{18}F -FDA (6). However, wide routine application of ^{11}C -HED is hampered by the short half-life of ^{11}C (20 min), because usually an individual radiosynthesis is required for each patient, and tracer distribution is not feasible (3). These limitations might be overcome by ^{18}F -FDA; however, its radiosynthesis is complex and its availability in clinical settings is limited (3). PET tracers targeting mechanisms other than norepinephrine uptake—for example, ^{18}F -FDOPA targeting the aromatic amino acid transporter and L-amino acid decarboxylase (3,7,8) and ^{68}Ga -labeled somatostatin analogs targeting somatostatin receptors (9)—have been successfully used for imaging of pheochromocytoma. However, their uptake mechanisms are different from substances specifically targeting the NET; therefore the quality of information delivered by these tracers, for example, regarding tumor characteristics, might be different. Overall, the clinical value of ^{18}F -LMI1195 remains to be evaluated in comparison with these tracers in future studies.

Desipramine-blocked rats showed significantly lower radioactivity accumulation in the bone, whereas activity in the liver and kidneys increased. These observations are most likely attributable to alterations in metabolism of ^{18}F -LMI1195 in desipramine-treated rats in vivo. However, it is a limitation of our study that in vivo metabolism of ^{18}F -LMI1195 has not been evaluated; thus the underlying mechanisms remain currently unclear.

BAT is highly innervated by sympathetic neurons and also accumulates catecholamines. Cold stimuli and catecholamines lead to growth and activation of BAT (22–24). Because it was not the focus of our studies, we did not include BAT in the biodistribution studies, and this is a limitation of our study. Furthermore, the experimental protocol used in the current study is error-prone regarding BAT analysis (e.g., lack of dedicated temperature control, among others). Thus in-depth analysis of BAT is not feasible using our current data and needs to be addressed in future studies using dedicated experimental protocols.

CONCLUSION

¹⁸F-LMI1195 shows high and specific uptake in endogenous pheochromocytomas developing in the MENX rat tumor model so that these lesions can be detected by PET imaging in vivo. SUV correlates with expression levels of the NET gene (*Scl6a2*) and with tumor volume. Tumor uptake of ¹⁸F-LMI1195 shows a strong correlation with ¹²³I-MIBG uptake and can be successfully blocked by the selective NET inhibitor desipramine. ¹⁸F-LMI1195 shows favorable biodistribution properties over ¹²³I-MIBG.

Altogether, our data suggest that ¹⁸F-LMI1195 is a promising tracer for diagnosis, staging, and follow-up of pheochromocytoma in patients.

Furthermore, we concluded that the MENX rat tumor model in combination with ¹⁸F-LMI1195 PET is an ideal platform to evaluate pheochromocytomas in vivo, which could be used for evaluation of novel antitumor drugs.

DISCLOSURE

The costs of publication of this article were defrayed in part by the payment of page charges. Therefore, and solely to indicate this fact, this article is hereby marked “advertisement” in accordance with 18 USC section 1734. This work has been supported by the Deutsche Forschungsgemeinschaft (DFG), Sonderforschungsbereich 824. Radiosynthesis of ¹⁸F-LMI1195 has been established in cooperation with Lantheus Medical Imaging Inc. Ming Yu and Simon Robinson are employees of Lantheus Medical Imaging Inc. No other potential conflict of interest relevant to this article was reported.

ACKNOWLEDGMENTS

We thank Sybille Reder, Marco Lehmann, and Markus Mittelhäuser for performing the PET scans; Annette Frank for cryosectioning, autoradiography, and microscopy; Michael Herz and Monika Beschoner for experimental support; and Dr. Iina Laitinen and Dr. Eliane Farrell for advice concerning autoradiography and animal handling.

REFERENCES

1. John H, Ziegler WH, Hauri D, Jaeger P. Pheochromocytomas: can malignant potential be predicted? *Urology*. 1999;53:679–683.
2. Manger WM, Gifford RW. Pheochromocytoma. *J Clin Hypertens (Greenwich)*. 2002;4:62–72.

3. Havekes B, Lai EW, Corssmit EP, Romijn JA, Timmers HJ, Pacak K. Detection and treatment of pheochromocytomas and paragangliomas: current standing of MIBG scintigraphy and future role of PET imaging. *Q J Nucl Med Mol Imaging*. 2008;52:419–429.
4. Yu M, Bozek J, Lamoy M, et al. Evaluation of LMI1195, a novel ¹⁸F-labeled cardiac neuronal PET imaging agent, in cells and animal models. *Circ Cardiovasc Imaging*. 2011;4:435–443.
5. Shulkin BL, Wieland DM, Schwaiger M, et al. PET scanning with hydroxyephedrine: an approach to the localization of pheochromocytoma. *J Nucl Med*. 1992;33:1125–1131.
6. Pacak K, Eisenhofer G, Carrasquillo JA, Chen CC, Li ST, Goldstein DS. ⁶-[¹⁸F] fluorodopamine positron emission tomographic (PET) scanning for diagnostic localization of pheochromocytoma. *Hypertension*. 2001;38:6–8.
7. Hoergerle S, Nitzsche E, Althoefer C, et al. Pheochromocytomas: detection with ¹⁸F DOPA whole body PET—initial results. *Radiology*. 2002;222:507–512.
8. Martinova L, Cleary S, Lai EW, et al. Usefulness of [¹⁸F]-DA and [¹⁸F]-DOPA for PET imaging in a mouse model of pheochromocytoma. *Nucl Med Biol*. 2012;39:215–226.
9. Win Z, Al-Nahhas A, Towey D, et al. ⁶⁸Ga-DOTATATE PET in neuroectodermal tumours: first experience. *Nucl Med Commun*. 2007;28:359–363.
10. Yu M, Bozek J, Lamoy M, et al. LMI1195 PET imaging in evaluation of regional cardiac sympathetic denervation and its potential role in antiarrhythmic drug treatment. *Eur J Nucl Med Mol Imaging*. 2012;39:1910–1919.
11. Pellegata NS, Quintanilla-Martinez L, Siggelkow H, et al. Germ-line mutations in p27Kip1 cause a multiple endocrine neoplasia syndrome in rats and humans. *Proc Natl Acad Sci USA*. 2006;103:15558–15563.
12. Fritz A, Walch A, Piotrowska K, et al. Recessive transmission of a multiple endocrine neoplasia syndrome in the rat. *Cancer Res*. 2002;62:3048–3051.
13. Molatore S, Liyanarachchi S, Irmeler M, et al. Pheochromocytoma in rats with multiple endocrine neoplasia (MENX) shares gene expression patterns with human pheochromocytoma. *Proc Natl Acad Sci USA*. 2010;107:18493–18498.
14. Miederer M, Molatore S, Marinoni I, et al. Functional imaging of pheochromocytoma with Ga-DOTATOC and C-HED in a genetically defined rat model of multiple endocrine neoplasia. *Int J Mol Imaging*. 2011;2011:175352.
15. Shilov M, Frey E, Segars P, Xu J, Tsui B. Improved Monte-Carlo simulations for dynamic PET [abstract]. *J Nucl Med*. 2006;47(suppl 1):197P.
16. Specht K, Richter T, Muller U, Walch A, Werner M, Hoffer H. Quantitative gene expression analysis in microdissected archival formalin-fixed and paraffin-embedded tumor tissue. *Am J Pathol*. 2001;158:419–429.
17. Verberne HJ, de Bruin K, Habraken JB, et al. No-carrier-added versus carrier-added ¹²³I-metaiodobenzylguanidine for the assessment of cardiac sympathetic nerve activity. *Eur J Nucl Med Mol Imaging*. 2006;33:483–490.
18. Higuchi T, Yousefi BH, Kaiser F, et al. Assessment of the ¹⁸F-labeled PET tracer LMI1195 for imaging norepinephrine handling in rat hearts. *J Nucl Med*. 2013;54:1142–1146.
19. Rischpler C, Fukushima K, Isoda T, et al. Discrepant uptake of the radiolabeled norepinephrine analogues hydroxyephedrine (HED) and metaiodobenzylguanidine (MIBG) in rat hearts. *Eur J Nucl Med Mol Imaging*. 2013;40:1077–1083.
20. Tomasi G, Turkheimer F, Aboagye E. Importance of quantification for the analysis of PET data in oncology: review of current methods and trends for the future. *Mol Imaging Biol*. 2012;14:131–146.
21. Garcia EV. Physical attributes, limitations, and future potential for PET and SPECT. *J Nucl Cardiol*. 2012;19(suppl 1):S19–S29.
22. Young P, Wilson S, Arch JR. Prolonged beta-adrenoceptor stimulation increases the amount of GDP-binding protein in brown adipose tissue mitochondria. *Life Sci*. 1984;34:1111–1117.
23. Ghorbani M, Claus TH, Himms-Hagen J. Hypertrophy of brown adipocytes in brown and white adipose tissues and reversal of diet-induced obesity in rats treated with a beta3-adrenoceptor agonist. *Biochem Pharmacol*. 1997;54:121–131.
24. Baba S, Engles JM, Huso DL, Ishimori T, Wahl RL. Comparison of uptake of multiple clinical radiotracers into brown adipose tissue under cold-stimulated and nonstimulated conditions. *J Nucl Med*. 2007;48:1715–1723.